Electronic Supplementary Material (ESI) for Journal of Materials Chemistry A.

Low Thermal Conductivity in $Bi_8CsO_8SeX_7$ (x = Cl, Br) by Combining Different Structural Motifs

J. A. Newnham, Q. D. Gibson, T.W. Surta, A. Morscher, T. D. Manning, L. M. Daniels, J.B. Claridge, and M. J. Rosseinsky

Contents

Rietveld fits of neutron diffraction patterns for $Bi_8CsO_8SeCl_7$ and $Bi_8CsO_8SeBr_7$

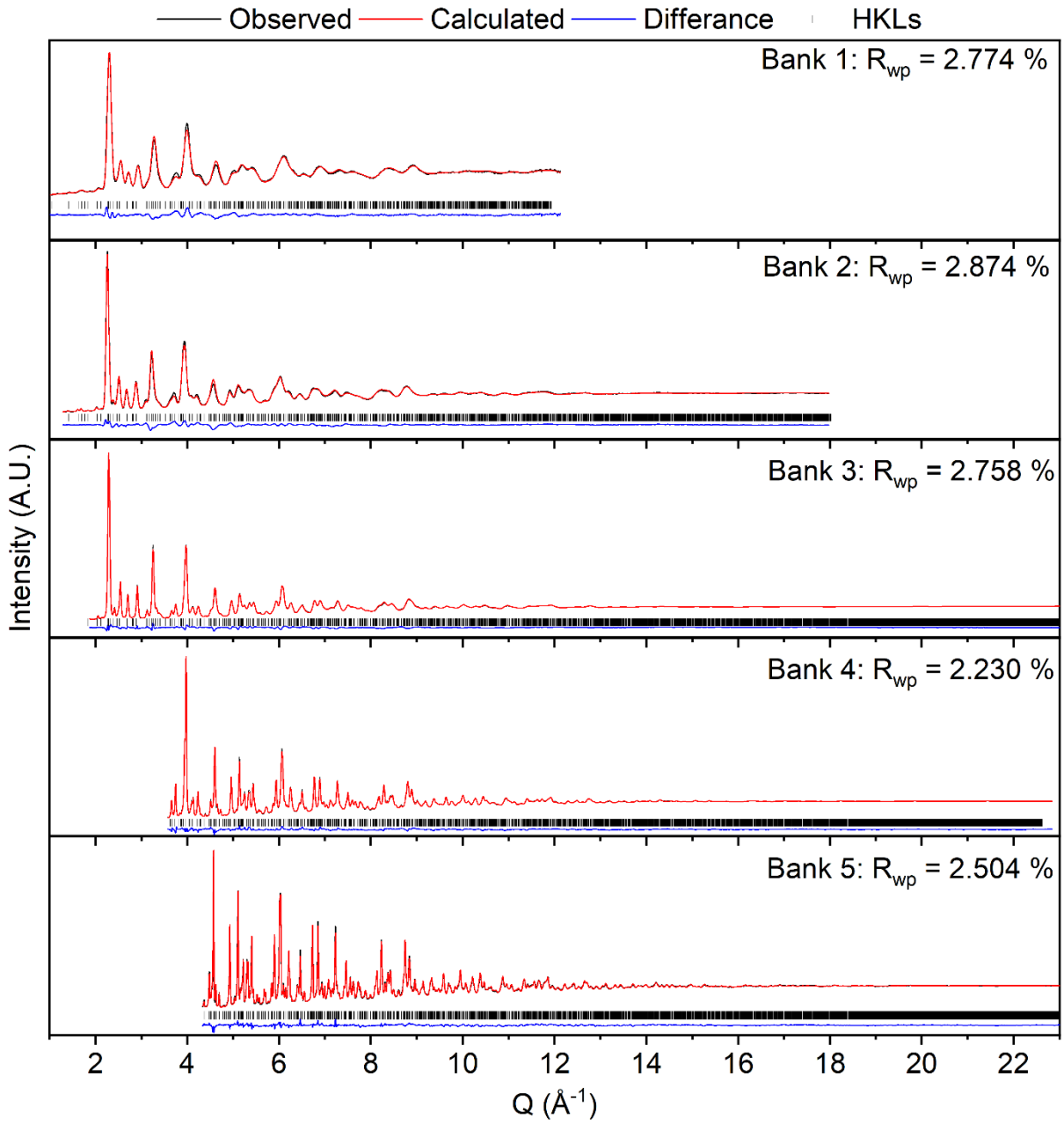

Figure S1: Rietveld refinements against neutron diffraction patterns of $Bi_8CsO_8SeCl_7$ measured at room temperature on NOMAD Banks 1-5. R_{wp} values are quoted as percentages (%).

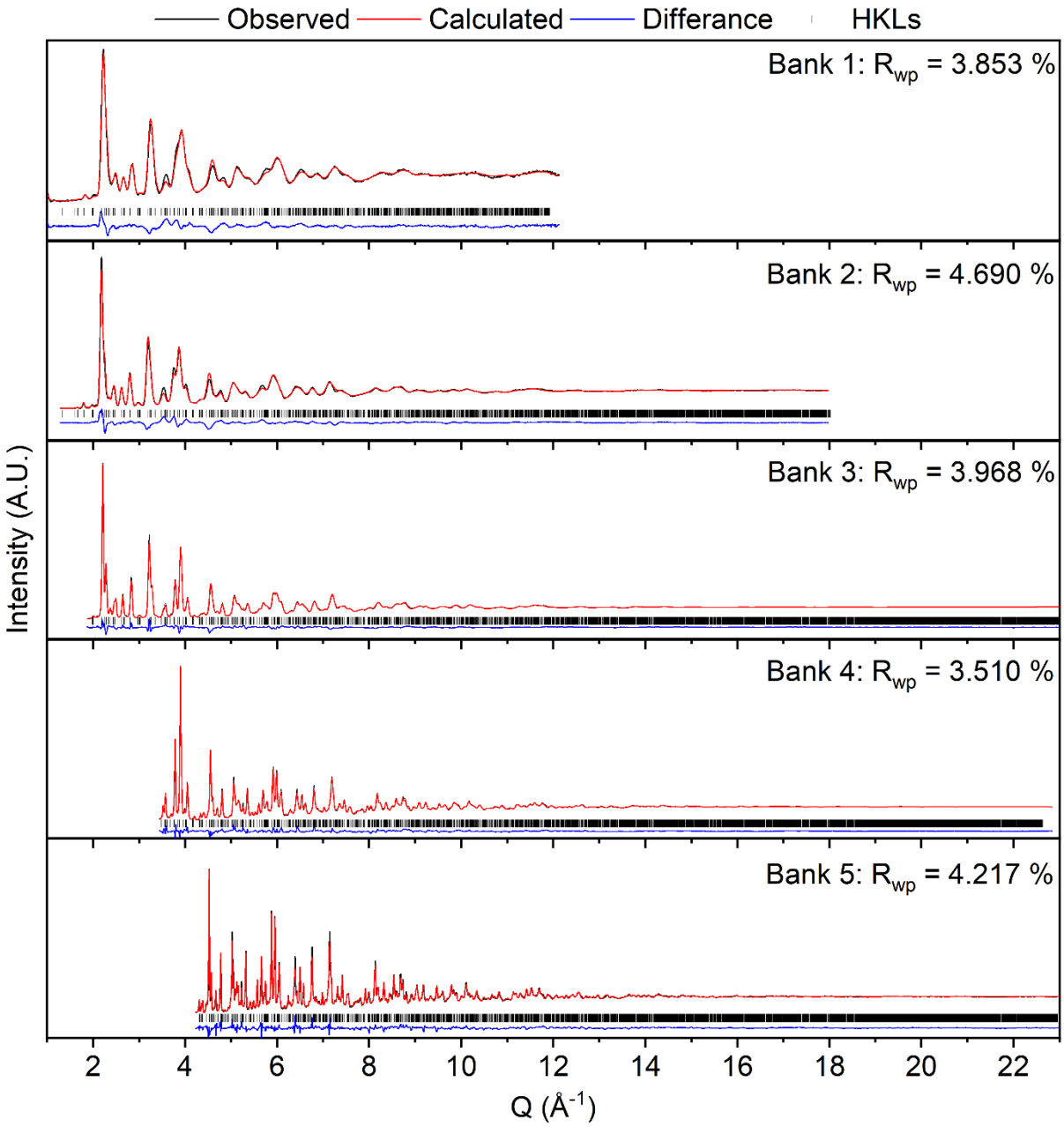

Figure S2: Rietveld refinements against neutron diffraction patterns of $Bi_8CsO_8SeBr_7$ measured at room temperature on NOMAD Banks 1-5.

Table S1: Structural parameters from Rietveld refinement against neutron diffraction data collected from $Bi_8CsO_8SeX_7$ (x = Cl and Br).

Phase	$Bi_8CsO_8SeCl_7$	$Bi_8CsO_8SeBr_7$
Space Group	*I*4/mmm	*I*4/mmm
Z	2	2
Temperature (K)	293.15	293.15
d spacing range (Å)	0.2659 - 6.2180	0.2659 – 6.2180
a (Å)	3.88778(3)	3.92996(5)
c (Å)	35.6002(8)	37.6653(11)
Volume ($Å^3$)	538.091(15)	581.73(2)
Density (g cm^{-3})	6.97	7.34
March Dollase Parameter (110)	0.827(2)	0.793(3)
R_{wp} (%)	2.725	4.0089

Table S2: Refined fractional atomic positions, occupancies and isotropic displacement parameters of $Bi_8CsO_8SeCl_7$ from neutron diffraction measurements.

Site	Atom	Wyckoff position	x	y	z	occupancy	U_{iso} ($Å^2$)
1	Bi	4e	0	0	0.11147(4)	1	0.0060(3)
2	Bi	4e	0	0	0.31809(4)	1	0.0119(4)
3	Cs	2a	0	0	0	0.5	0.0090(8)
4	Cl	4e	0.5	0.5	0.06618(3)	1.0	0.0163(3)
5	Cl	4e	0	0	0.21817(4)	0.750(16)	0.0108(2)
5	Se	4e	0	0	0.21817(4)	0.250(16)	0.0108(2)
6	O	8g	0.5	0	0.14449(4)	1	0.0067(2)

Table S3: Refined fractional atomic positions, occupancies and isotropic displacement parameters of $Bi_8CsO_8SeBr_7$ from neutron diffraction measurements.

Site	Atom	Wyckoff position	x	y	z	occupancy	U_{iso} ($Å^2$)
1	Bi	4e	0	0	0.11206(5)	1	0.0060(3)
2	Bi	4e	0	0	0.32225(6)	1	0.0089(4)
3	Cs	2a	0	0	0	0.5	0.0073(11)
4	Br	4e	0.5	0.5	0.06532(6)	0.980(6)	0.0185(5)
4	Se	4e	0.5	0.5	0.06532(6)	0.020(6)	0.0185(5)
5	Br	4e	0	0	0.21756(5)	0.770(6)	0.0139(4)
5	Se	4e	0	0	0.21756(5)	0.230(6)	0.0139(4)
6	O	8g	0.5	0	0.14376(5)	1	0.0063(2)

The displacement parameters where initially modelled anisotropically, however it produced U_{11}s and U_{33}s that where within error of each other indicating that each site should be modelled isotropically. As such, the displacement parameters where refined isotopically for the remainder of the refinement.

Diffraction Patterns of $Bi_8Cs_xO_8Se_xCl_{8-x}$

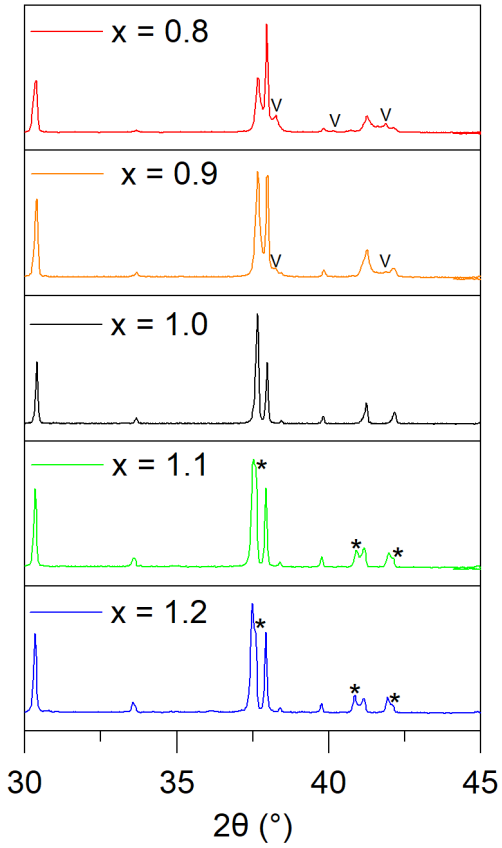

Figure S3: Powder X-ray diffraction patterns of $Bi_8Cs_xO_8Se_xCl_{8-x}$ (x = 0.8, 0.9, 1.0, 1.1, 1.2). Two unidentified impurity phases are marked as "v" and "*", respectively.

Bi-Cs-Se-X (X = Cl, Br) quaternary plots

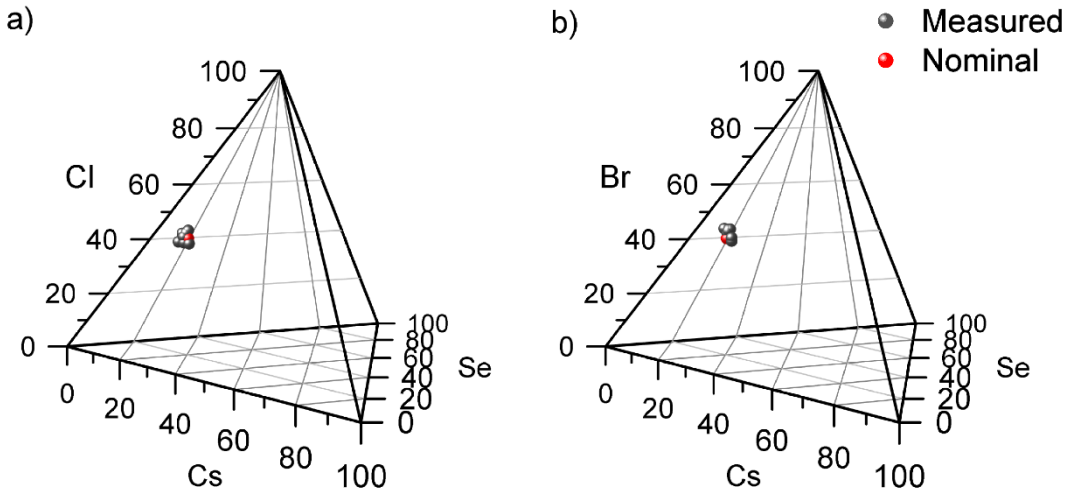

Figure S4: Bi-Cs-Se-X (X = Cl, Br) quaternary plots graphing the measured compositions of a) $Bi_8CsO_8SeCl_7$ and b) $Bi_8CsO_8SeBr_7$ by TEM-EDX.

Attempted Synthesis of $Bi_4CsO_4SeCl_3$ and $Bi_8CsO_8Se_3Cl_3$

Attempts to prepare $Bi_4CsO_4SeCl_3$ and $Bi_8CsO_8Se_3Cl_3$ were made using the same synthetic procedures as those use to make $Bi_8CsO_8SeCl_7$. This involved using stoichiometric amounts of Bi_2O_3, Bi_2Se_3, CsCl and BiOCl, and heating them at 700 °C in an evacuated quartz ampule. These materials were targeted based on simultaneous Pb^{2+}-for-Bi^{3+} and Cl^{-}-for-Se^{2-} substitutions in the known materials $Pb_{0.6}Bi_{1.4}Cs_{0.6}O_2Cl_2$ and $Pb_{1.5}Bi_{2.5}Cs_{0.5}O_4Cl_3$. There was no evidence of the homologous target forming in the PXRD patterns from these initial conditions as all peaks in the PXRD patterns could be accounted for by $Bi_8CsO_8SeCl_7$, Bi_2O_2Se, and CsCl.

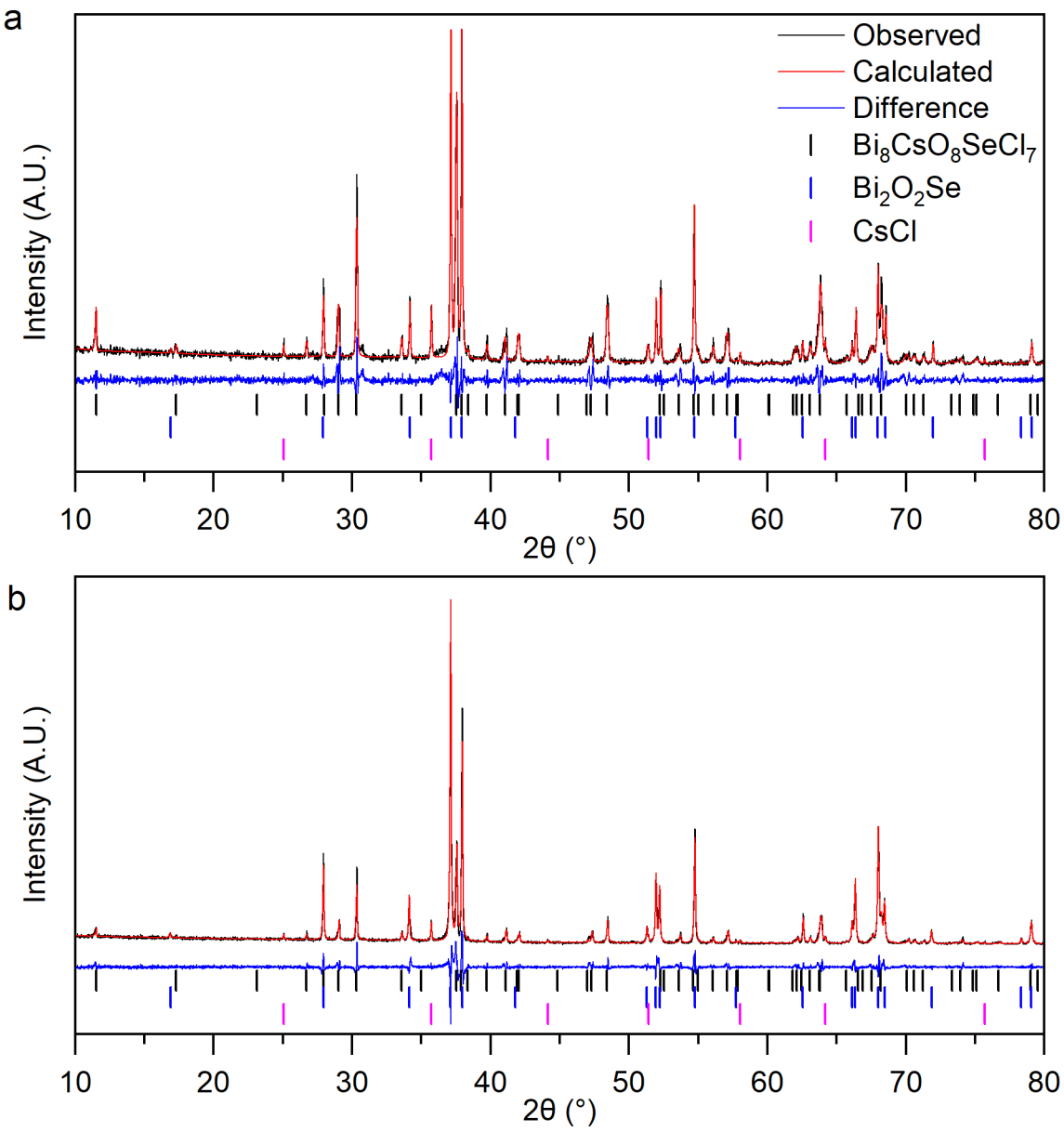

Figure S5: PXRD patterns and Pawley fits of the products from the attempted synthesis of a) $Bi_4CsO_4SeCl_3$ and b) $Bi_8CsO_8Se_3Cl_3$, showing that all peaks can be indexed to the phases $Bi_8CsO_8SeCl_7$, Bi_2O_2Se, and CsCl.

Thermal and Water Stability of $Bi_8CsO_8SeX_7$ (x = Cl, Br)

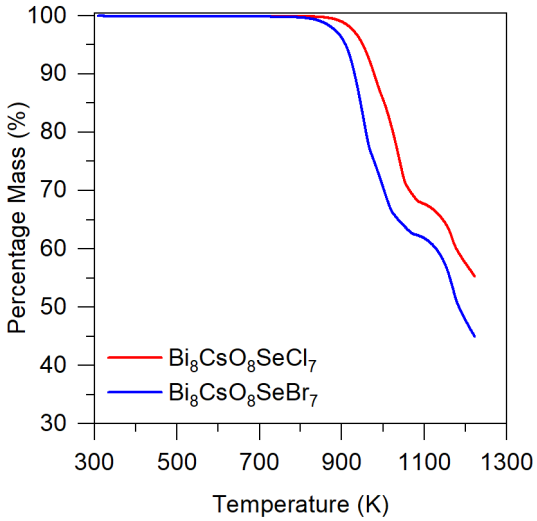

Figure S6: Mass loss curves of $Bi_8CsO_8SeX_7$ from thermogravimetric analysis under flowing N_2.

Table S4: Lattice parameters of $Bi_8CsO_8SeX_7$ (X = Cl and Br) before and after sonication in water for 24 hours.

Material	Treatment	a (Å)	c (Å)
$Bi_8CsO_8SeCl_7$	Before Sonication	3.88781(4)	35.6002(7)
	After Sonication	3.88906(7)	35.7542(8)
$Bi_8CsO_8SeBr_7$	Before Sonication	3.92996(5)	37.6653(11)
	After Sonication	3.93013(7)	37.9710(8)

Table S5: The compositions of $Bi_8CsO_8SeX_7$ (X = Cl and Br) as determined by TEM-EDX measurements before and after the powders where pressed by spark plasma sintering.

	$Bi_8CsO_8SeCl_7$			
	Bi	Cs	Se	Cl
As Synthesised	8.0(3)	0.7(3)	0.96(6)	6.9(5)
After SPS	8.0(2)	1.1(3)	0.9(1)	7.3(2)

	$Bi_8CsO_8SeBr_7$			
	Bi	Cs	Se	Br
As Synthesised	8.0(2)	0.9(3)	0.97(4)	7.6(4)
After SPS	8.0(2)	1.3(3)	0.96(8)	7.3(1)

Diffraction Pattern of a Dense Pellet of $Bi_8CsO_8SeCl_7$

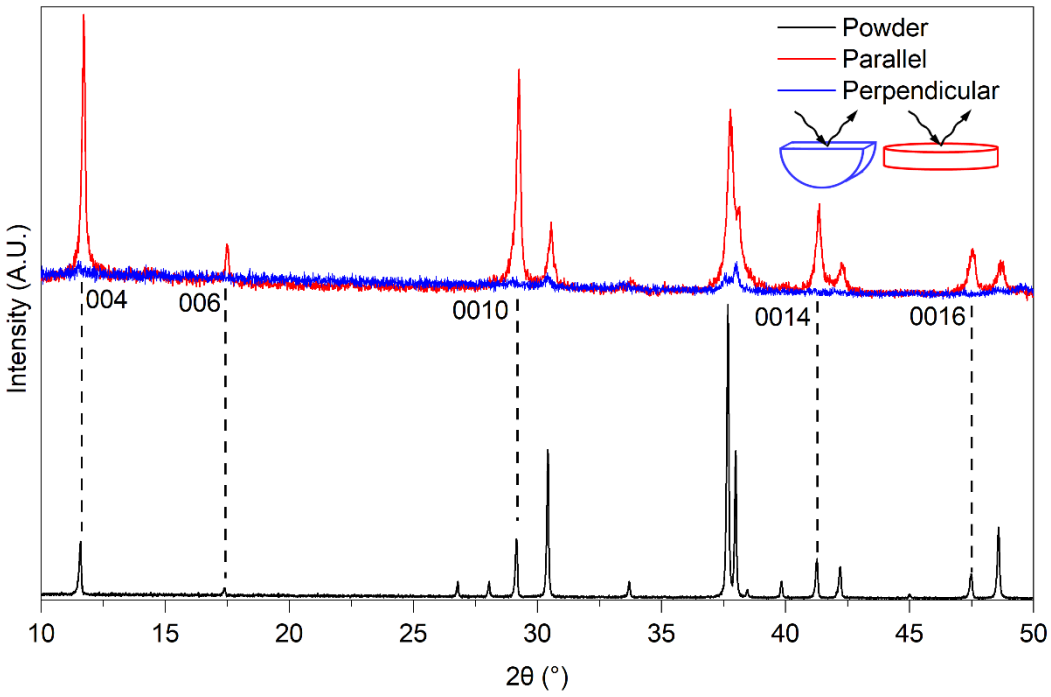

Figure S7: Powder X-ray diffraction pattern of a pellet of $Bi_8CsO_8SeCl_7$ measured parallel and perpendicular to the SPS pressing direction. Shown in the inset, the perpendicular measurement was made by cutting a pellet in half and measuring the cut face. The 00*l* peaks are labelled to highlight their enhanced relative intensity in the parallel pattern relative to those in a powder pattern. This results from texturing within the sintered pellet as the pressing direction aligns parallel with the c-axis of the unit cell. The intensity of the peaks in the perpendicular pattern are small due to the small area of the pellet cross section (8 × 1 mm), but nevertheless shows a suppression of the 00*l* peaks compared to the parallel measurement.

Thermal Conductivity of $Bi_8CsO_8SeX_7$ up to 600 K

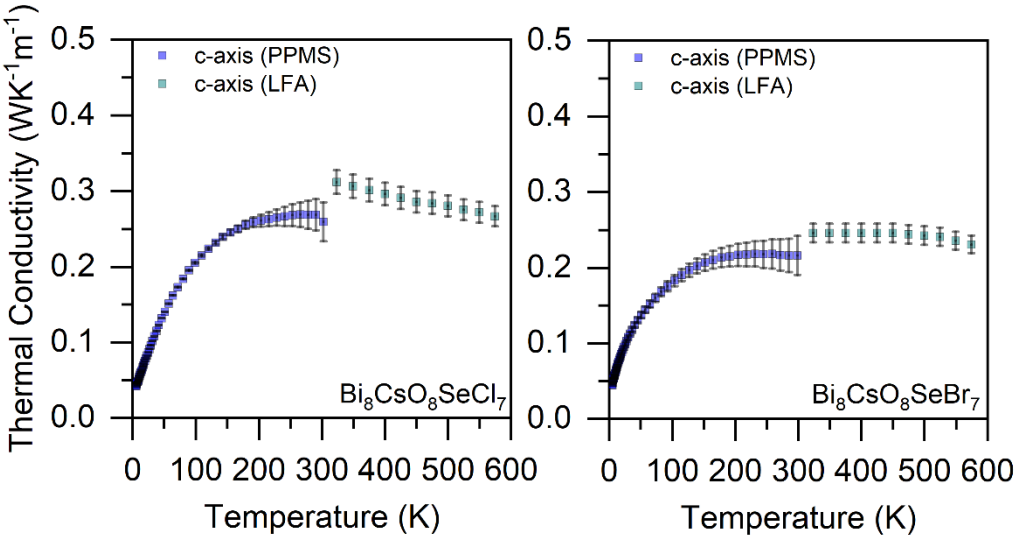

Figure S8: The thermal conductivity of $Bi_8CsO_8SeCl_7$ and $Bi_8CsO_8SeBr_7$ when measured up to 600 K by laser flash analysis parallel to the pressing direction using a Netzsch LFA 457. Measurements

were made under dynamic vacuum with a heating rate of 3 K min^{-1} with 5 min equilibration at each temperature. Thermal diffusivities were obtained by fitting the Cowan model to raw data. The thermal conductivities were then obtained multiplying the thermal diffusivity, sample density, and heat capacity (assumed to be 3R at high temperatures).

Heat Capacity Model and Refined Parameters

To extract the Debye and Einstein temperatures associated with each material, the heat capacity $C_P(T)$ of each material was modelled by a linear combination of Debye and Einstein functions.

$$C_P(T) = \sum_i a_i \, C_{Di}(T) + \sum_i b_i \, C_{Ei}(T) + \gamma T \quad \text{(S1)}$$

where C_D, C_E and γ represent the Debye, Einstein, and linear contributions to the heat capacity respectively. a_i and b_i are pre-factors that are normalised to sum to one, and γ is the Sommerfeld coefficient. The Debye contributions to the heat capacity (C_D) were calculated using:

$$C_D(T) = 9R\left(\frac{T}{\theta_D}\right)^3 \int_0^{\frac{T}{\theta_D}} \frac{x^4 e^x}{(e^x - 1)^2} dx \quad \text{(S2)}$$

In which R is the ideal gas constant, and θ_D is the refined Debye temperature. The Einstein contributions (C_E) were calculated using:

$$C_E(T) = 3R\left(\frac{\theta_E}{T}\right)^2 \frac{e^{\frac{\theta_E}{T}}}{\left(e^{\frac{\theta_E}{T}} - 1\right)^2} \quad \text{(S3)}$$

In which θ_E is the refined Einstein temperature.

Table S6: The refined parameters in fitting the heat capacities of $Bi_8CsO_8SeCl_7$ and $Bi_8CsO_8SeBr_7$.

	$Bi_8CsO_8SeCl_7$	$Bi_8CsO_8SeBr_7$
a_1	0.45	0.53
θ_{D1} (K)	180(10)	150(10)
a_2	0.48031	0.43282
θ_{D2} (K)	555(10)	510(10)
b_1	0.060	0.032
θ_{E1} (K)	59(2)	52(2)
b_2	0.0092	0.0049
θ_{E2} (K)	29(2)	25(2)
b_3	0.00049	0.00028
θ_{E3} (K)	12(1)	12(1)
γ ($JK^{-2}mol^{-1}$)	0.00031	0.00049

The Debye temperatures extracted from the heat capacity data are corroborated by the value determined from separate analysis of isotropic displacement parameters as a function of temperature (Figure 3).

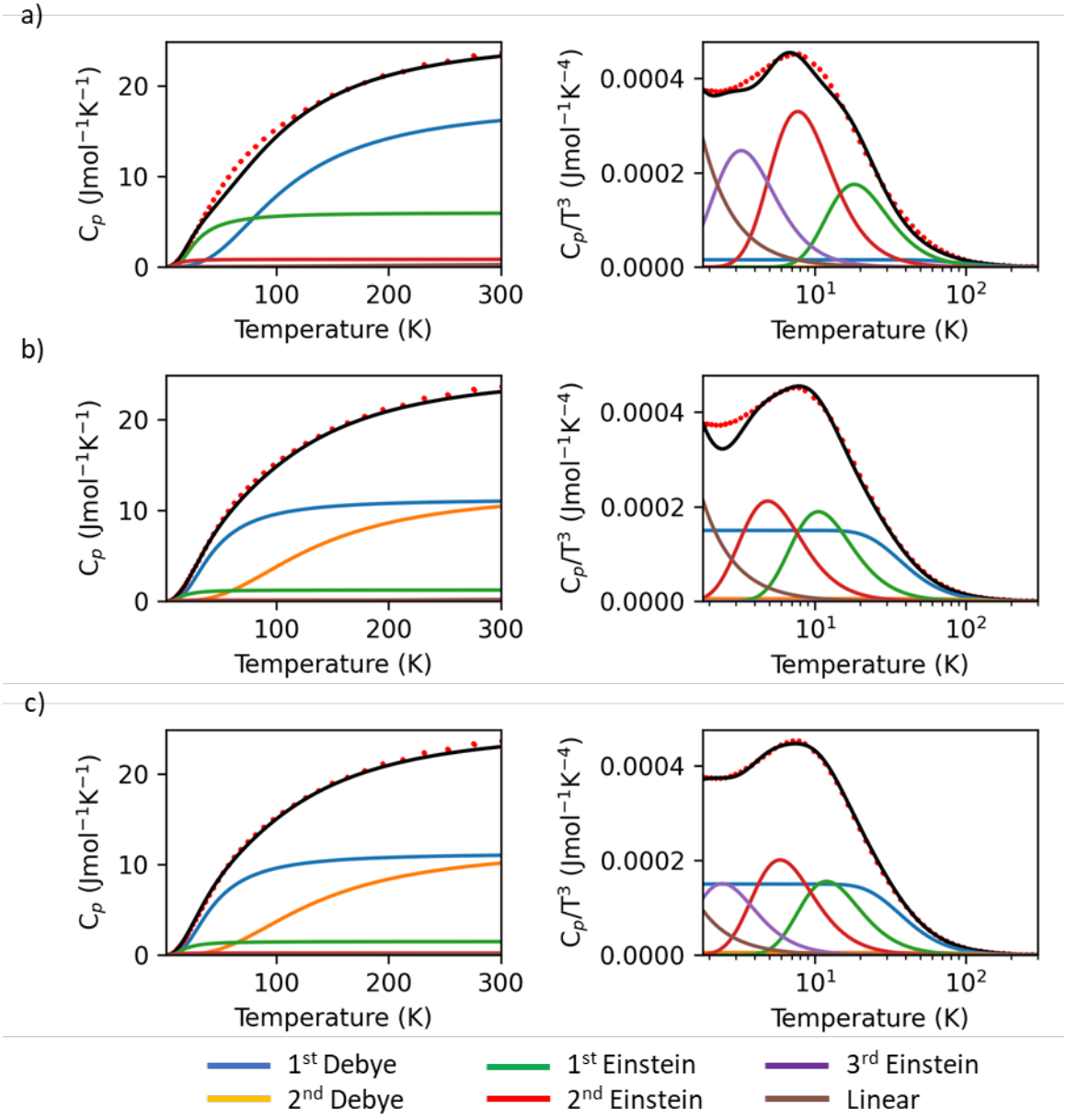

Figure S9: The heat capacity of $Bi_8CsO_8SeCl_7$ cannot accurately be fit with fewer than 2 Debye and 3 Einstein temperatures. For example, lower quality fits are shown with a) 1 Debye and 3 Einstein temperatures, or b) 2 Debye and 2 Einstein temperatures. c) The fit of the heat capacity data with all parameters included (2 Debye and 3 Einstein) is shown for comparison.

Experiments Investigating the origin of large U_{iso} in $Bi_8CsO_8SeCl_7$

Table S7: The refined isotropic displacement parameters (U_{iso}) of each site in $Bi_8CsO_8SeCl_7$ at different temperatures extracted from synchrotron VT-PXRD data.

	U_{iso} (Å^2)				
Temperature (K)	Bi(1)	Bi(2)	Cs	$Cl_{0.75}Se_{0.25}$	Cl
100	0.0023(3)	0.0108(3)	0.0226(13)	0.0052(8)	0.0104(15)
150	0.0032(3)	0.0125(3)	0.0254(14)	0.0071(8)	0.0161(17)
200	0.0040(3)	0.0137(3)	0.0295(15)	0.0085(8)	0.0200(19)
250	0.0058(3)	0.0155(3)	0.0352(15)	0.0102(8)	0.0228(19)
300	0.0065(3)	0.0174(4)	0.0441(17)	0.0122(9)	0.023(2)
350	0.0062(3)	0.0219(4)	0.0470(19)	0.0161(10)	0.023(2)
400	0.0091(4)	0.0234(5)	0.055(2)	0.0189(11)	0.025(2)
450	0.0108(4)	0.0254(5)	0.059(2)	0.0201(11)	0.028(2)
500	0.0121(4)	0.0279(5)	0.063(2)	0.0230(12)	0.032(2)

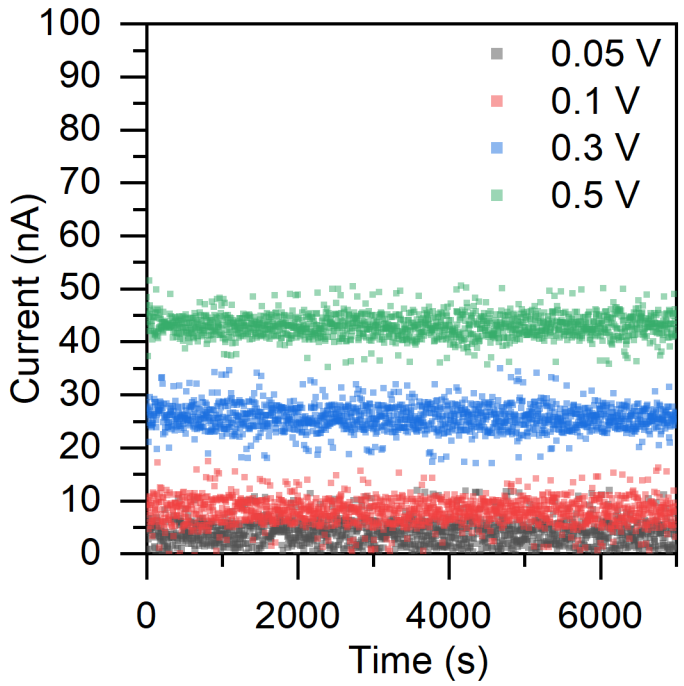

Figure S10: The DC polarisation data of $Bi_8CsO_8SeCl_7$ at 0.05, 0.1, 0.3, and 0.5 V.

Observed Fourier Maps of $Bi_8CsO_8SeCl_7$

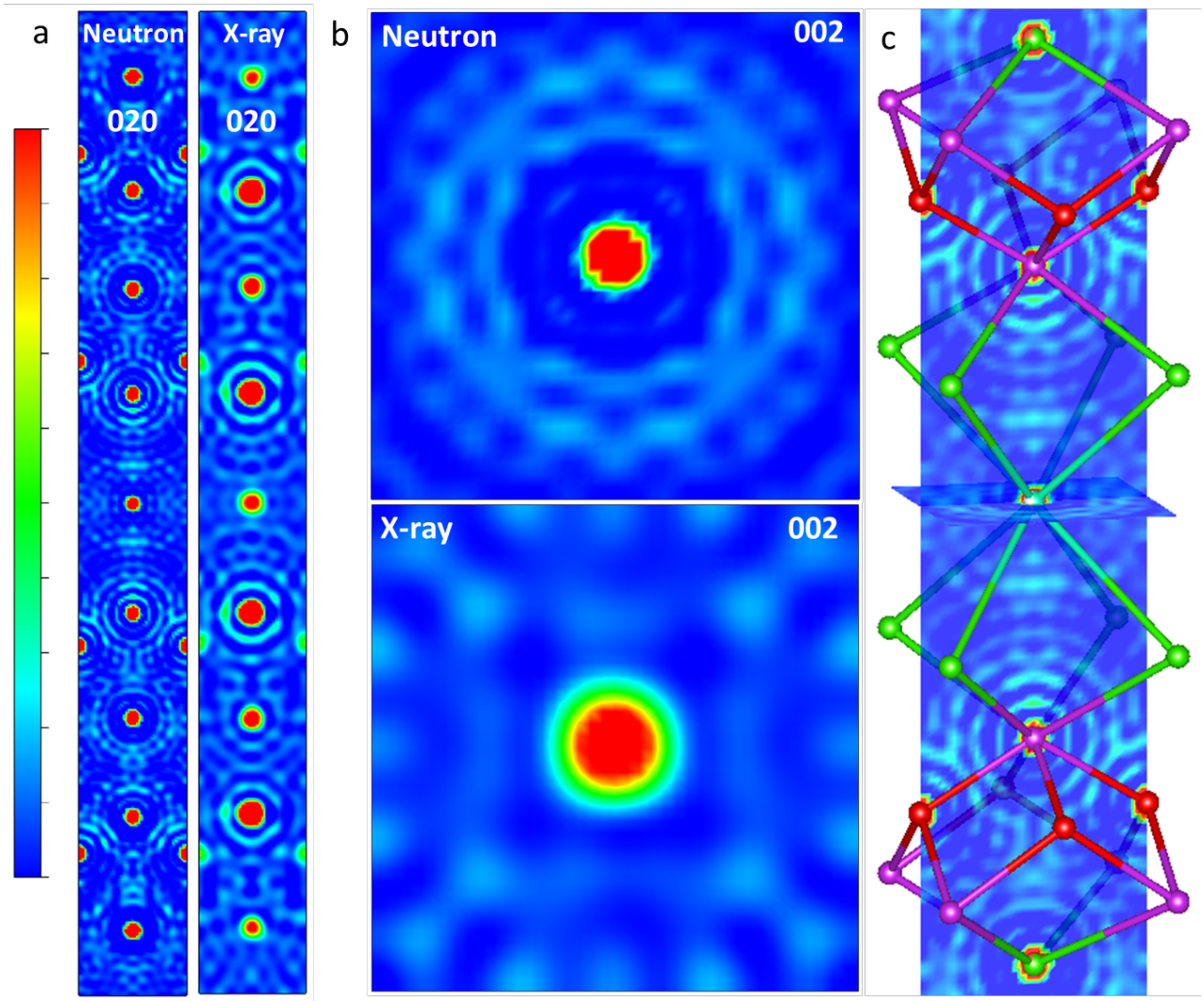

Figure S11: The observed Fourier maps along the (a) 020 and (b) 002 planes calculated using the neutron diffraction data from NOMAD Bank 5, and also with synchrotron PXRD. (c) The observed Fourier maps along both the 002 and 020 planes overlaid with the refined structure of one layer of $Bi_8CsO_8SeCl_7$.

Thermal Conductivity Model and Refined Parameters

The thermal conductivities in the text were modelled using the Debye-Callaway Model. The thermal conductivity (κ) of a material can be written as the product of a material's density of states (g), heat capacity (C), and thermal diffusivity (α), all as a function of frequency.

$$\kappa(\omega) = g(\omega)C(\omega)\alpha(\omega) \tag{S4}$$

The Debye heat capacity can be derived from the density of states $g(\omega)$ to give:

$$C(T) = 9Nk_B\left(\frac{T}{\theta_D}\right)\int_0^{\frac{T}{\theta_D}} \frac{x^4 e^x}{(e^x - 1)}\,dx \tag{S5}$$

where N is the atomic number density. The minimum thermal diffusivity can then be calculated in terms of the phonon mean free path (l_{mfp}):

$$\alpha_{min}(\omega) = \frac{v l_{mfp}}{3} = \frac{v^2\pi}{3\omega} \tag{S6}$$

here, v is the phonon velocity, and $l_{mfp} = \pi v/\omega = 0.5$ phonon wavelength, the smallest length a phonon can meaningfully be. Parametrising $\alpha_{min}(\omega)$ in terms of *T* where

$$T = \frac{k_B}{\hbar\omega} \tag{S7}$$

and substituting S7 and S5 into S4 gives the minimum thermal conductivity κ_{min} per phonon polarisation:

$$\kappa_{min}(T) = \left(\frac{\pi}{6}\right)^{1/3} k_B N^{\frac{2}{3}} v\left(\frac{T}{\theta_D}\right)^2 \int_0^{\frac{T}{\theta_D}} \frac{x^3 e^x}{(e^x - 1)}\,dx \tag{S8}$$

where $x = \frac{\hbar\omega}{k_B T}$. To obtain a full model for $\kappa(T)$, the scattering length is then allowed to vary based on the total scattering lifetime, $l_{mfp} = v\tau(\omega)$, and is calculated:

$$\tau(\omega)^{-1} = \tau_{PD}(\omega)^{-1} + \tau_{ED}(\omega)^{-1} + \tau_U(\omega)^{-1} + \tau_{Res}(\omega)^{-1} + \tau_B(\omega)^{-1} \tag{S9}$$

Each of the terms in Equation S9 are scattering processes, and are given respectively below.

Point Defect Scattering:

$$\tau_{PD}(\omega)^{-1} = A\omega^4 \tag{S10}$$

Extended Defect Scattering:

$$\tau_{ED}(\omega)^{-1} = B\omega^2 \tag{S11}$$

Umklapp Scattering:

$$\tau_U(\omega)^{-1} = U\omega^2 T e^{-\frac{\theta_D}{3T}} \tag{S12}$$

Resonant Scattering:

$$\tau_{res}(\omega)^{-1} = \frac{Q\omega^2{\omega_E}^4}{(\omega^2-\omega_E^2)+\gamma^2\omega_E^2\omega^2} \quad \text{(S13)}$$

Boundary Scattering:

$$\tau_B(\omega)^{-1} = \frac{v_D}{l_B} \quad \text{(S14)}$$

In the above; *A*, *B*, *U*, and *Q* are the refined pre-factors for fitting the thermal conductivity. ω_E is an Einstein frequency related to the Einstein temperatures extracted from the heat capacity fits, and *γ* is a dampening term that can vary from 0 to 1. As *γ* is unknown in these materials it was fixed to 0.5.

As multiple good fits could be obtained using different values for each pre-factor, the *A* pre-factor was constrained to be within error of its theoretical value, which was in turn calculated using:

$$\tau_{PD}(\omega)^{-1} = \frac{V}{4\pi v^3}\left(\sum_i f_i\left(1-\frac{m_i}{\bar{m}}\right)^2 + \sum_i f_i\left(1-\frac{r_i}{\bar{r}}\right)^2\right)\omega^4 = A\omega^4 \quad \text{(S15)}$$

where *V* is the volume per atom, f_i is the fraction of atoms with mass m_i and radius r_i on a crystallographic site with average mass $\bar{m}$ and radius $\bar{r}$. This gave a value of $A = 9.1(3) \times 10^{-41}$ s^3 for $Bi_8CsO_8SeCl_7$ and $A = 1.1(3) \times 10^{-40}$ s^3 for $Bi_8CsO_8SeBr_7$. Substituting $l_{mfp} = v\tau(\omega)$ into Equation S6 gives the contribution towards the thermal diffusivity proportional to the phonon lifetime:

$$\alpha_{lifetime}(\omega) = \frac{v^2\tau(\omega)^{-1}}{3} \quad \text{(S16)}$$

Again parametrising $\alpha_{lifetime}(\omega)$ in terms of *T*, and substituting S5 and S16 into S4 gives the phonon lifetime component of thermal conductivity per phonon polarisation.

$$\kappa_{lifetime}(T) = Nk_B v^2\left(\frac{T}{\theta_D}\right)^2\int_0^{\frac{T}{\theta_D}}\frac{\tau(T)x^4e^x}{(e^x-1)}dx \quad \text{(S17)}$$

The equation for $\kappa(T)$ per phonon polarisation mode is obtained by summing the minimum and lifetime components of the thermal conductivity.

$$\kappa(T) = \kappa_{min}(T) + \kappa_{lifetime}(T) \quad \text{(S18)}$$

To obtain the full model used in the text, each term in Equation S18 is multiplied by a factor of 3 to account of the 3 polarisation modes (two transverse and one longitudinal). As there are also multiple Debye temperatures (θ_{Di}) that contribute to the heat capacity and in turn towards the thermal conductivity, each contribution is multiplied with its respective pre-factors (a_i) from Equation S1 and are summed.

$$\kappa(T) = \sum_i a_i 3(\kappa_{min,i}(T) + \kappa_{lifetime,i}(T)) \quad \text{(S19)}$$

In the above model, the mean phonon velocities were calculated using equation S20 and the Debye temperatures extracted from the models of the heat capacity (Figure 2 and Table S6). These are given in table 8.

$$v = \frac{\theta_D k_B}{\hbar (6\pi^2 N)^{\frac{1}{3}}} \quad \text{(S20)}$$

Table S8: The phonon velocities used in the thermal conductivity model as calculated from the Debye temperatures extracted from the heat capacity fits.

Material	Debye Temperature (K)	Phonon Velocity (ms^{-1})
$Bi_8CsO_8SeCl_7$	180(10)	1680(90)
	555(10)	5190(90)
$Bi_8CsO_8SeBr_7$	150(10)	1440(90)
	510(10)	4890(90)

Einstein contributions to the heat capacity were not included in the final equation for κ as they represent localised vibrational modes and therefore do not contribute towards the thermal conductivity. The out-of-plane thermal conductivities were also not modelled as they require the optical phonon cut-off frequencies and the acoustic phonon velocities in order to obtain a κ_{min} that is smaller than $\kappa_{Observed}$. These are obtainable through DFT calculations but are not required for this study. We also note that, because the electronic conductivities of the materials are low, ~1.4×10^{-6} S cm^{-1}, the electronic contribution towards the total thermal conductivity is negligible as, using the Wiedemann–Franz law, it was estimated to be 1.0×10^{-9} W K^{-1} m^{-1} at 300 K. Therefore, it was not included in the model as the measured thermal conductivities represent κ_{latt}.

Table S9: The parameters used for modelling the thermal conductivity of $Bi_8CsO_8SeCl_7$ along the *ab*-plane (perpendicular to the pressing direction).

$A(\times 10^{-41} s^3)$	$B(\times 10^{-16} s)$	$U(\times 10^{-18} s)$	$Q_{59K}(\times 10^{11})$	$l_B(\times 10^{-6} m)$
9.1(2)	5.0(2)	9.6(2)	2.4(2)	2.0(5)

Table S10: The parameters used for modelling the thermal conductivity of $Bi_8CsO_8SeBr_7$ along the *ab*-plane (perpendicular to the pressing direction).

$A(\times 10^{-40} s^3)$	$B(\times 10^{-15} s)$	$U(\times 10^{-16} s)$	$Q_{52K}(\times 10^{11})$	$l_B(\times 10^{-6} m)$
1.4(2)	1.4(2)	4.2(2)	3.1(2)	2.0(5)

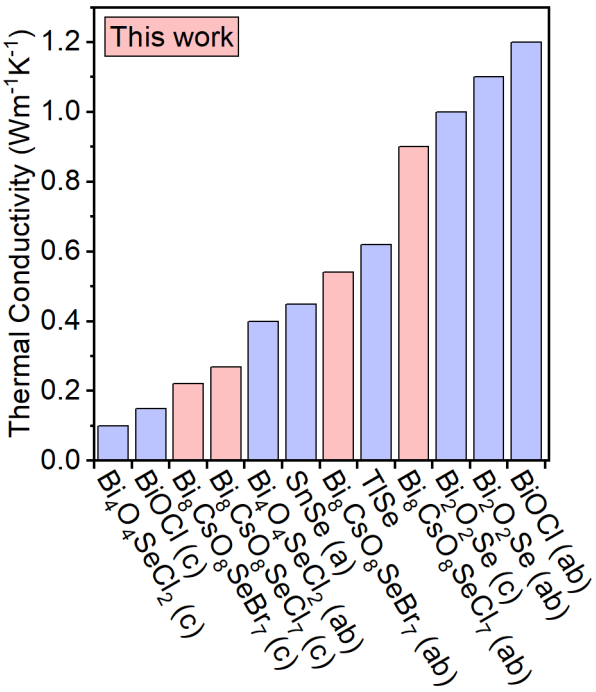

Figure S12: The low thermal conductivities of $Bi_8CsO_8SeX_7$ in comparison to other low thermal conductivity materials with similar chemistries at room temperature.[1–3]

PXRD Pattern of $Bi_{3.4}Pb_{0.6}Cs_{0.6}O_4Cl_4$

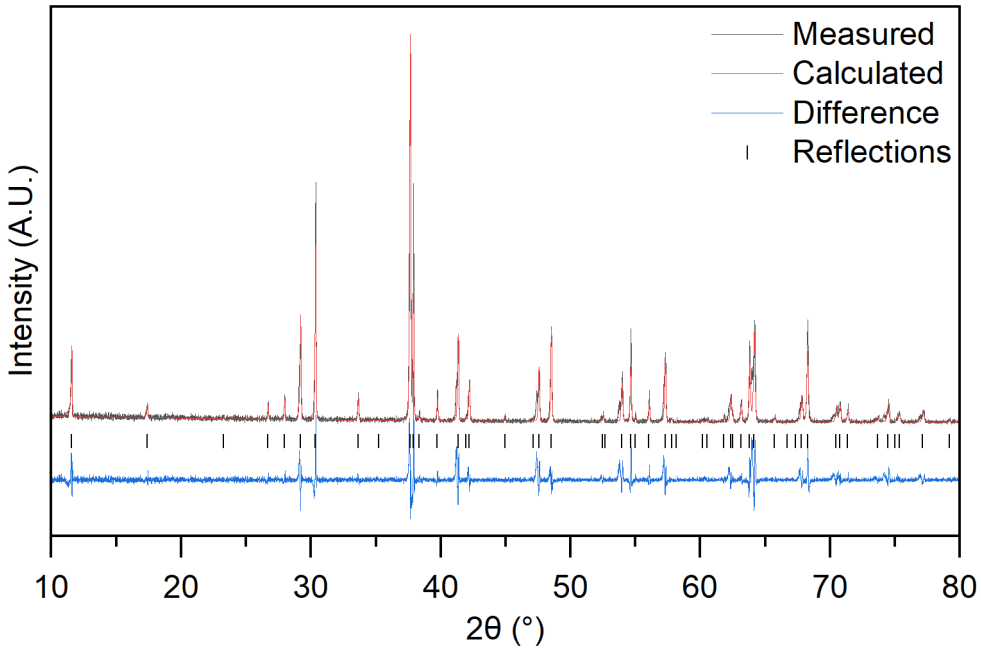

Figure S13: PXRD patterns and Pawley fits from the synthesis of $Bi_{3.4}Pb_{0.6}Cs_{0.6}O_4Cl_4$ with the measured calculated, and difference plotted as black red and blue lines respectively.

References

1 Q. D. Gibson, T. Zhao, L. M. Daniels, H. C. Walker, R. Daou, S. Hébert, M. Zanella, M. S. Dyer, J. B. Claridge, B. Slater, M. W. Gaultois, F. Corà, J. Alaria and M. J. Rosseinsky, *Science.*, 2021, **373**, 1017–1022.

2 M. Dutta, S. Matteppanavar, M. V.D. Prasad, J. Pandey, A. Warankar, P. Mandal, A. Soni, U. V. Waghmare and K. Biswas, *J. Am. Chem. Soc.*, 2019, **141**, 20293–20299.

3 X.-L. Shi, W.-D. Liu, M. Li, Q. Sun, S.-D. Xu, D. Du, J. Zou, Z.-G. Chen, X.-L. Shi, Z.-G. Chen, W.-D. Liu, M. Li, S.-D. Xu, D. Du, J. Zou and Q. Sun, *Adv. Energy Mater.*, 2022, **12**, 2200670.